



A sulfur-poor terrestrial core inferred from metal–silicate partitioning experiments



Terry-Ann Suer^{a,*}, Julien Siebert^{b,**}, Laurent Remusat^a, Nicolas Menguy^a,
Guillaume Fiquet^a

^a Institut de Minéralogie, de Physique des Matériaux, et de Cosmochimie (IMPMC) Sorbonne Universités - UPMC Univ Paris 06, UMR CNRS 7590, Museum National d'Histoire Naturelle, IRD, 4 Place Jussieu, F-75005 Paris, France

^b Institut de Physique du Globe de Paris, Sorbonne Paris Cité - Université Paris Diderot, UMR CNRS 7154, F-75005 Paris, France

ARTICLE INFO

Article history:

Received 12 December 2016

Received in revised form 11 April 2017

Accepted 11 April 2017

Available online 3 May 2017

Editor: J. Brodholt

Keywords:

sulfur

core formation

metal–silicate partitioning

diamond anvil cell

quantitative NanoSIMS analyses

ABSTRACT

As a siderophile and a volatile element, sulfur's partitioning behavior allows constraints to be placed on processes in the primitive Earth. Sulfur's core–mantle distribution during Earth's accretion has consequences for core content and implications for volatile accretion. In this study, metal–silicate partitioning experiments of sulfur were conducted in a diamond anvil cell at pressures from 46 to 91 GPa and temperatures between 3100 and 4100 K, conditions that are directly relevant to core segregation in a deep magma ocean. The sulfur partition coefficients measured from these experiments are an order of magnitude less than those obtained from extrapolation of previous results to core formation conditions (e.g., Rose-Weston et al., 2009; Boujibar et al., 2014). These measurements challenge the idea that sulfur becomes a highly siderophile element at high pressures and temperatures. A relationship was derived that describes sulfur's partitioning behavior at the pressure–temperature range of core formation. This relationship combined with an accretion model was used to explore the effects of varying impactor sizes and volatile compositions on the sulfur contents of the Earth's core and mantle. The results show that homogeneous delivery of sulfur throughout accretion would overenrich the mantle in sulfur relative to the present day observations of 200 ± 80 ppm (Lorand et al., 2013) unless the bulk Earth sulfur content is lower than its cosmochemical estimate of ~ 6400 ppm (e.g., McDonough, 2003). On the other hand, the mantle's sulfur content is matched if sulfur is delivered with large bodies (3 to 10% Earth mass) during the last 20% of Earth's accretion, combined with a chondritic late veneer of 0.5% Earth mass. These results are conditional on the lowered equilibration efficiency of large impactor cores in a terrestrial magma ocean. In each accretion scenario, the core sulfur content remains below ~ 2 wt.% in close agreement with cosmochemical estimates and is a further indication that sulfur is not a dominant light element in the core.

© 2017 Elsevier B.V. All rights reserved.

1. Introduction

Metal–silicate partitioning studies provide constraints on the relative proportion of elements that entered the Earth's core and mantle during differentiation (e.g., Righter et al., 1997; Wade and Wood, 2005). The relatively low abundance of sulfur in the bulk silicate Earth (200 ± 80 ppm, Lorand et al., 2013) is commonly attributed to its strong partitioning into liquid iron during core formation (Li and Agee, 2001; Rose-Weston et al., 2009). This deduc-

* Corresponding author.

** Corresponding author.

E-mail addresses: terry-ann.suer@impmc.upmc.fr (T.-A. Suer), siebert@ipgp.fr (J. Siebert).

tion also provides a convenient solution to the core density deficit problem and several works have explored the possibility of sulfur as a light element in the core (e.g., Ahrens, 1979). Estimates for the core sulfur content are derived from either cosmochemical mass balance considerations (e.g., McDonough and Sun, 1995) or from comparison of the physical properties of (Fe, S) alloys at high pressure and high temperature with geophysical models of the core (e.g., Badro et al., 2014; Morard et al., 2013). Sulfur's depletion in the mantle with respect to lithophile elements of comparable volatilities such as Zn argues for a maximum of 2 wt.% sulfur in the core (McDonough, 2003). However, a sulfur-rich core was proposed by Seagle et al. (2006) (up to 15 wt.%) from Fe₃S equation of state measurements while Morard et al. (2013) suggested a core containing 6 wt.% sulfur from direct liquid-metal density measurements at megabar pressures. Reassessment of the siderophile

behavior of Zn also leads to a core richer in sulfur (Mahan et al., 2017). In contrast, Badro et al. (2014) predicted from experiments and *ab initio* calculations that a core deprived of sulfur is a better match for geophysical observations (i.e. sound velocity, density). Several studies have also shown that silicon and oxygen provide a better match than sulfur as light elements in the core (e.g., Alfe et al., 2000; Siebert et al., 2013).

The near-chondritic proportions of the chalcogens (S, Te, Se) in the Earth's mantle indicates a chondritic origin for these elements (Wang and Becker, 2013). The mantle's sulfur content is generally assumed to have been delivered along with other volatiles with an oxidized late veneer (Albarede, 2009; Wang and Becker, 2013). However, in order to explain the depletion of the chalcogens relative to other moderately volatiles such as Zn and Pb, these elements must have been present to some extent during the main stages of Earth's accretion (Halliday, 2013; Wood, 2008). A pre-late veneer presence of volatiles is also required to explain the isotopic signatures of S, Ag and Cu (Labidi et al., 2013; Schönbachler et al., 2010; Savage et al., 2015) and the mantle abundances of siderophile elements W and Mo (Wade et al., 2012) which are attributed to core–mantle equilibrium. The partially devolatilized early building blocks of the Earth could have delivered minor amounts of sulfur but it has also been suggested that large impactors towards the end of accretion could have brought sulfur and other volatiles (Wohlert and Wood, 2015). Dynamical models have suggested that volatile-rich material derived from the outer solar system was added to the Earth during late accretion (Raymond et al., 2006; Morbidelli et al., 2012). Models which explore the outcome of different histories for volatile delivery to the Earth can place broad constraints on the timing and origin of volatile accretion. But in order to evaluate the core–mantle distribution of volatile sulfur during accretion, accurate knowledge of its partitioning behavior during core formation is required.

Several studies have been conducted with large volume presses to quantify sulfur's partitioning behavior (e.g., Li and Agee, 2001; Rose-Weston et al., 2009; Boujibar et al., 2014). There is a general agreement that sulfur becomes more siderophile with increasing pressure while temperature has the opposite effect (Li and Agee, 1996, 2001; Mavrogenes and O'Neill, 1999; Rose-Weston et al., 2009; Boujibar et al., 2014). However, estimates of the magnitude of pressure and temperature effects vary among studies. Sulfur's increasing affinity for iron with depth argues for it being present in the core as a dominant light element (Li and Agee, 2001) and for a late veneer origin of sulfur in the silicate Earth from chondritic materials (Rose-Weston et al., 2009; Wang and Becker, 2013). It has also been shown that sulfur becomes more lithophile at low oxygen fugacities (Rose-Weston et al., 2009; Boujibar et al., 2014). Consequently, heterogeneous accretion models involving reduced conditions in the earliest phases of accretion (e.g. Wade and Wood, 2005; Schönbachler et al., 2010) yield final mantle sulfur content which is higher than observed (see Boujibar et al., 2014 for further details). Addition of sulfur in the later stages of accretion provides a possible solution to this issue while raising the abundances of some siderophile elements like W in the mantle to their current levels through a large effect of sulfur on metal–silicate partitioning (Wade et al., 2012). No systematic study has been done on sulfur partitioning at pressures above 25 GPa or temperatures higher than 2400 K. Yet estimates of core formation conditions include pressures between 45 to 65 GPa and temperatures up to 4000 K (e.g., Wade and Wood, 2005; Rubie et al., 2011; Siebert et al., 2012).

In this work, metal–silicate partitioning experiments of sulfur were conducted at pressures from 46 to 91 GPa and temperatures between 3100 and 4100 K. Sulfur partitioning was quantified as a function of pressure, temperature and liquid metal composition.

A general partition function was obtained from fitting a multiple linear regression model to a dataset which combines the results of this study with those of previous works. This partitioning function was applied to a core formation model to constrain the cumulative amount of sulfur which partitioned into the core and the mantle throughout accretion. The model takes into account different impactor sizes, changes in volatile compositions of impactor material over time and varying equilibration efficiency between impactor core and the Earth's mantle. The challenge of precisely quantifying the chemical composition in diamond anvil cell run products for such supposedly highly siderophile element at conditions of our experiments is addressed by the use of Nanoscale Secondary Ion Mass Spectroscopy (NanoSIMS). NanoSIMS provides both the spatial resolution (~ 300 nm) and analytical resolution suitable for measuring the low sulfur content dissolved in the silicate quenched melt region of the run products. Transmission electron microscopy (TEM) was also used to probe the structure and composition of metallic and silicate melts.

2. Methods

2.1. Starting material

The metallic starting material consisted of a thin foil of iron alloyed with 3 to 6 wt.% sulfur. Two starting silicate compositions were used as magma ocean analogs: A natural MORB (Mid Oceanic Ridge Basalt) from the East Pacific Rise in seven experiments, and a peridotite glass of KLB-1 composition synthesized by aerodynamic levitation laser furnace used in two experiments. Table A.4 reports starting material compositions.

Silicate starting materials were polished down to 15–20 μm in thickness and the (Fe,S) alloys to ~ 10 μm , which were machined with a femtosecond laser instrument into small disks. Each experiment was prepared by placing a piece of alloy, 10 to 15 μm in diameter, between two silicate platelets of 60 to 80 μm in diameter inside a laser drilled rhenium sample chamber that was pre-indented to 30 to 40 μm . The silicate acts as a pressure medium and a chemical and thermal insulator (Fiquet et al., 2010). A small ruby was placed at the edge of the sample chamber to obtain pressure readings by ruby fluorescence (Mao et al., 1978).

2.2. Laser heated diamond anvil cell experiments

The experiments were performed in diamond anvil cells equipped with culet anvils of 200 or 250 μm in diameter, coupled with a double-sided 200 W fiber laser ($\lambda = 1070$ nm). The laser (spot size 10 to 20 μm) was focused on the contact between the alloy and the silicate from both sides. Spectra of the radiation emitted (range 500 to 750 nm) from the heated region were recorded from the two sides of the DAC simultaneously and temperatures determined by fitting the emission with a Planck function (Boehler, 2000). The temperature was ramped up quickly until a significant fraction of material in the region of the laser focus was molten at which point the temperature stabilized, Fig. 1. This temperature behavior has also been noted by several previous works (Andrault et al., 2011; Siebert et al., 2012; Fiquet et al., 2010). All experiments were carried out at superliquidus conditions at run times between 45 s and 2 min, sufficient to reach chemical equilibrium at the length scales of DAC experiments (Siebert et al., 2012). Cutting the laser power quenched the experiments. The post quench pressures were determined by ruby fluorescence and were corrected for thermal pressure with a value of $\Delta P_{th} \sim 2.5 \cdot 10^{-3}$ GPa/K as used in previous works (Fiquet et al., 2010; Siebert et al., 2012).

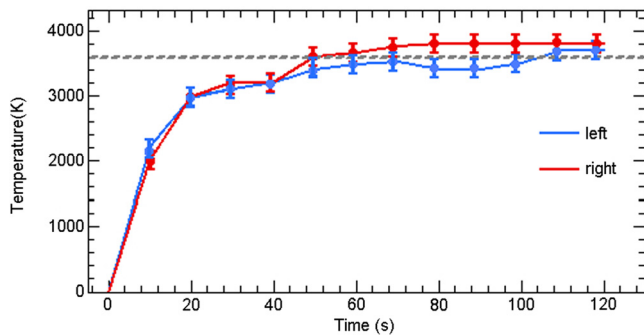


Fig. 1. Temperature as a function of time measured from the two sides of the cell during laser heating. The laser power is increased rapidly during the first 10 s to increase the temperature and induce melting of the sample at the laser focus. The plateau corresponds to the silicate solidus. Samples are kept molten for between 45 s and 2 min.

2.3. Sample recovery

A focus ion beam (FIB) was used to recover thin sections of 3 to 5 μm in thickness, and 20 to 30 μm in length and width from the quenched molten regions of each sample, characterized by a metallic blob 5 to 10 μm in diameter, surrounded by a quenched liquid silicate pocket of several microns in extent (Fig. 2). Rims of crystals and unreacted silicate surround the molten region. The sections were deposited onto a 5 cm^2 silicon wafer by a tungsten needle attached to a micromanipulator.

2.4. Compositional analysis

The major element composition of the samples was characterized by energy dispersive X-ray analysis (EDX) with a Zeiss Cross-beam field emission gun (FEG) – Scanning electron microscopy (SEM). Typical operating conditions include an accelerating voltage of 15 keV. The spectra were measured from regions of interests that are several μm^2 in size from both the silicate and metal during 60 s integrations. The major and minor element compositions were cross-checked with a CAMECA SX 100 electron microprobe. Operating conditions included an accelerating voltage of 15 keV, beam current of 10 nA, a spot size of 1 to 5 μm and counting times of 10–20 s on peak and background. Several oxides and pure metals were used as internal standards for the measurements: diopside (Si, Mg Ca), Fe_2O_3 (Fe), orthoclase (K, Al), albite (Na), MnTiO_3 (Ti, Mn), Cr_2O_3 (Cr), and pyrite FeS_2 (Fe, S).

The quenched silicates liquid in these experiments can have complicated fine structures as shown in Fig. 2. Obtaining high precision, spatially resolved measurements of trace species from these small areas is challenging with standard petrologic tools. Previous works (e.g., Siebert et al., 2013; Fischer et al., 2015) have used WDX or EDX spectroscopy with an electron microprobe (EMP) or a transmission electron microscope (TEM) to quantify compositions in quench products of DAC experiments. As sulfur was predicted to be highly siderophile at high pressure, neither of these techniques were capable of achieving the required analytical and spatial resolutions to quantify sulfur at a few tens of ppm at the micrometer scale. We measured sulfur concentration in the silicate regions with a CAMECA NanoSIMS 50 installed at the Museum National d'Histoire Naturelle (IMPMC-MNHN), Paris.

The NanoSIMS uses a finely focused primary beam to erode the top atomic layers of the target material and produce secondary ions which are analyzed by a high-resolution multi-collection mass spectrometer (Hoppe et al., 2013). The DAC samples were measured by NanoSIMS during three sessions in which secondary ions of $^{16}\text{O}^-$, $^{28}\text{Si}^-$, $^{32}\text{S}^-$, $^{43}\text{AlO}^-$ and $^{56}\text{Fe}^-$ were recorded. The mass resolving power (MRP) of the instrument was sufficient to distinguish the species of interest from major interferences, for example

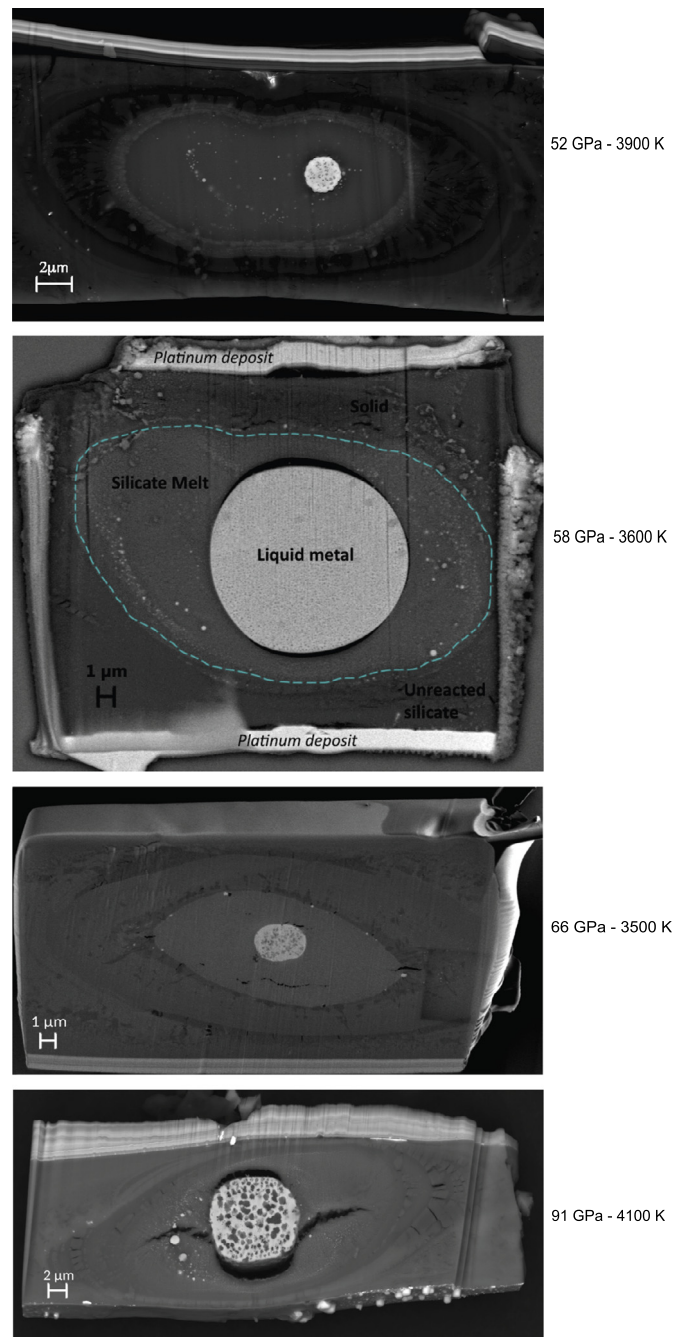


Fig. 2. SEM image of four thin sections for experimental run products #3, #2, #6, #9 respectively. All samples show the morphology typical of quench metal–silicate partitioning experiments. A metallic blob in a quench silicate liquid pocket surrounded by unreacted starting material. In some samples cracks are seen in the silicate phases. A space can be seen at interface between metal and silicate in some samples. These cracks and spaces are likely due to mechanical stresses incurred during decompression of the cell. Light grey areas around the lamellae are deposits of platinum which protect sample during ion milling.

$^{32}\text{S}^-$ and $^{16}\text{O}_2^-$. Precisely controlled raster of the primary beam across the sample surface produced high-resolution ion maps. The ion images were analyzed with the software L'Image (Larry Nittler, Carnegie Institution for Science). Regions of interest (ROIs), 1 to 2 μm^2 in area, were defined and measurements of the sulfur/silicon ratio extracted. The high resolution of the NanoSIMS maps, allowed small zones to be selected for analysis (Fig. 3).

The sub-micron structure of one sample (experiment #9) was probed by TEM. The sample was thinned by FIB to ~ 50 nm and

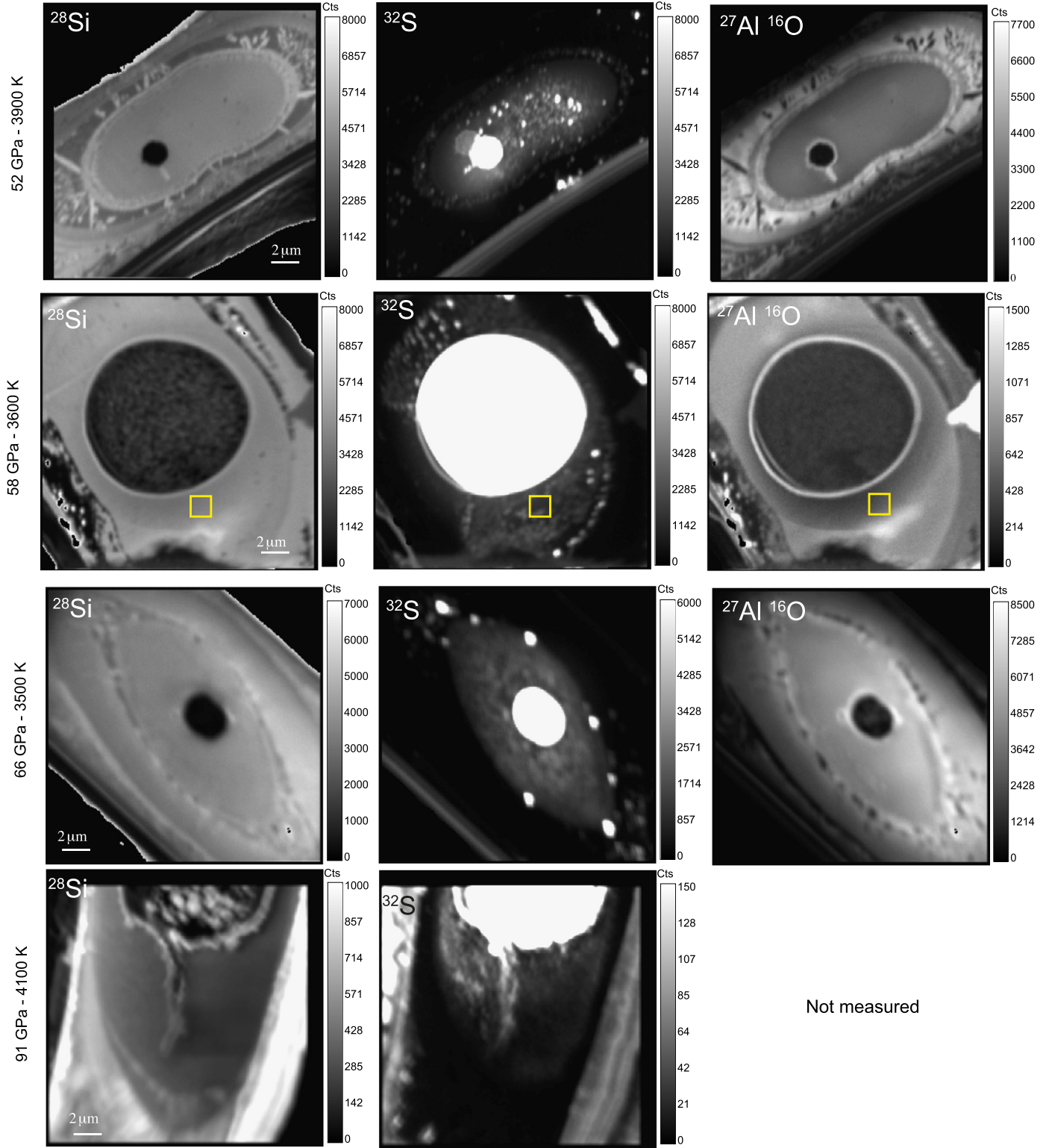


Fig. 3. NanoSIMS chemical maps in greyscale. Samples are shown in the same order as Fig. 2 but with each sample being rotated. The box shows the typical size of ROIs from which compositions are extracted. Sulfur map shows the metallic blob as white due to saturation in the scaling of measurements for display. There is a correlation between the metal rich areas and sulfur rich regions while the presence of AlO_3 corresponds to the silicate regions.

analyzed with a JEOL 2100F TEM operating at 200 kV in several modes. High angle annular dark field (HAADF) imaging mode, Fig. 4a and d; Energy Dispersive X-ray (STEM-EDX) mode, Fig. 4b, c, e, and f. Electron diffraction patterns were also collected from some features.

3. Results

3.1. General appearance

A central metallic blob and a surrounding quenched silicate liquid pocket is evident in all of the experimental run products (ex-

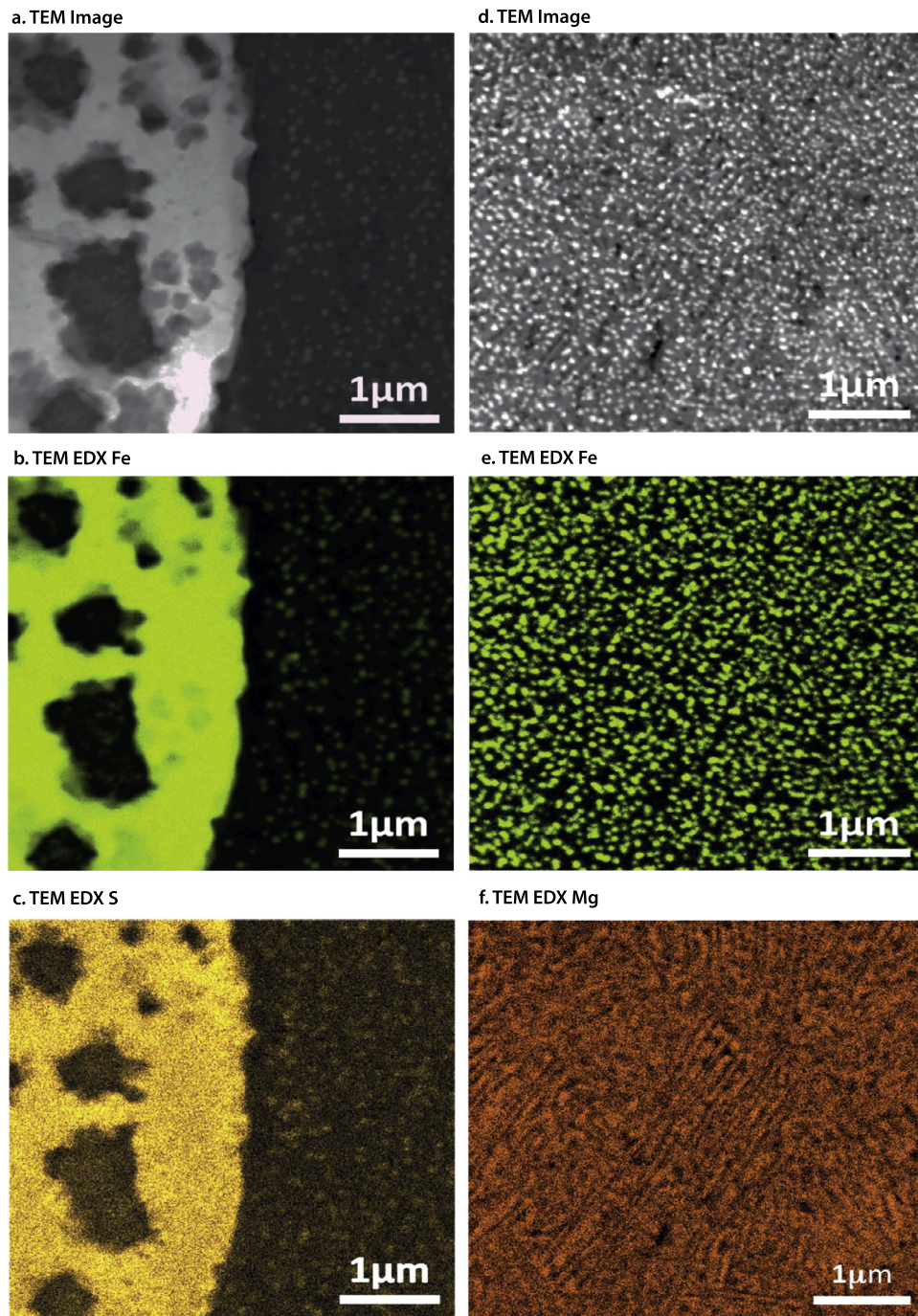


Fig. 4. TEM observations of the interface between metallic blob and quench silicate liquid for run #9. a. Dark field image, b. EDX Fe, c. EDX S, d. Dark field image, e. EDX Fe, f. EDX Mg. There is a correlation between the occurrence of iron and sulfur. Elongated crystals evident in the EDX magnesium map are due to the quench from high temperatures.

amples in Fig. 2). This appearance is consistent with previous superliquidus metal–silicate partitioning experiments performed on siderophile elements in diamond anvil cells (e.g., Siebert et al., 2012, 2013; Fischer et al., 2015). Similar features have been reported, though at larger scales, by studies done in large volume cell experiments (e.g., Kilburn and Wood, 1997; Rose-Weston et al., 2009; Boujibar et al., 2014).

Three populations of metals are observed in the run products: the largest metal blob, 4 to up to 15 μm is the main reservoir of iron and siderophile elements while the medium sized blobs (hundreds of nanometers) are metal fragments that did not coalesce before the experiment was quenched. The ~ 50 nm sized grains

that are ubiquitous in the quenched silicate are interpreted as exsolutions from the molten silicate during quench, Fig. 4b.

3.2. Quench texture

Petrological textures consistent with rapid quench of liquids from high temperatures are expressed in the metal and silicate run products. The main metal blobs can exhibit two distinct textures; circular exsolutions of several tens of nanometers in diameter and larger, irregularly shaped exsolutions. Fig. 2 shows this diversity of metal textures which have also been seen in previous studies (e.g., Siebert et al., 2012). EDX mapping under TEM of one ir-

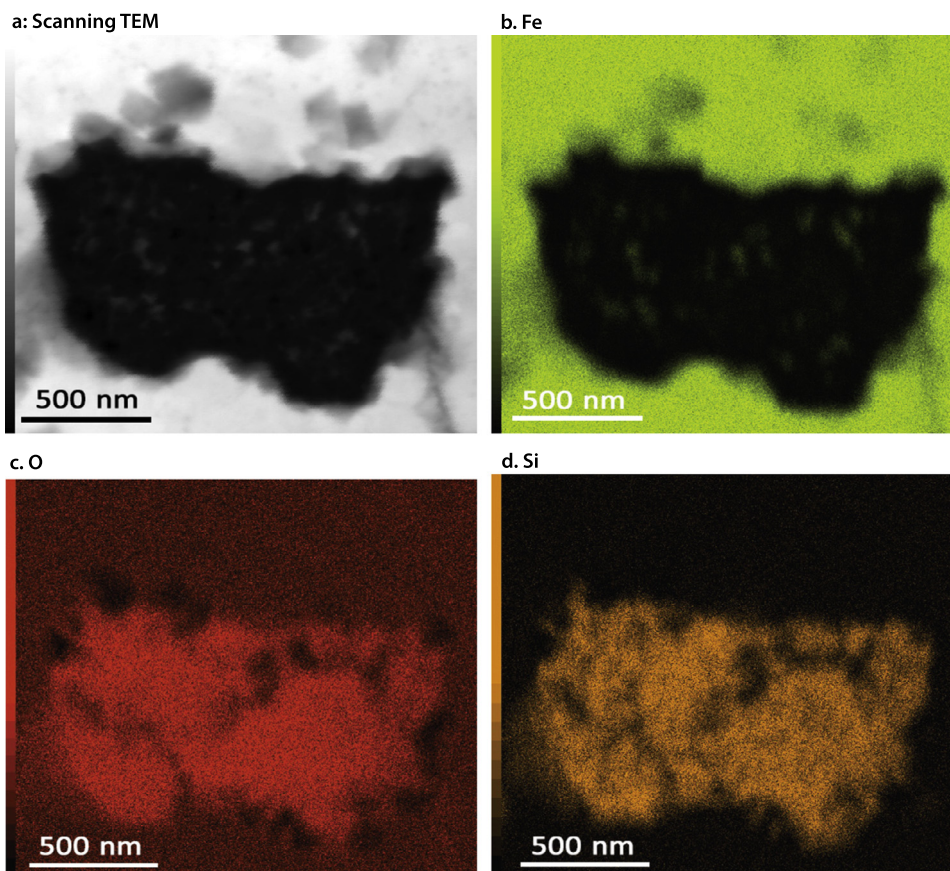


Fig. 5. TEM observations of an irregular quench feature present in the metal blob of one experiment (Run #9). Brighter colors indicate higher concentrations. The feature is enriched in oxygen and silicon. a. STEM HAADF image, b. STEM EDX Fe, c. STEM EDX O, d. STEM Si.

regularly textured region (from experiment #9) shows that these features are silicon and oxygen rich (Fig. 5) and probably exsolved during the quench. These TEM observation supports the hypothesis that these elements are increasingly soluble in liquid iron at higher temperatures and pressures (Siebert et al., 2012). The silicate quench displays elongated textures on submicron scales when examined by TEM EDX, shown in the magnesium map, Fig. 4f. Such textures are interpreted as the result of rapid cooling of a silicate liquid from high temperatures (e.g., Chabot and Agee, 2003; Boujibar et al., 2014).

TEM imaging and EDX mapping of experiment #9 (Fig. 4) show that the ~50 nm sized grains are iron rich and contains significant amounts of sulfur. Analysis of electron diffraction patterns was not conclusive due to the small size of these grains which are embedded in surrounding silicate phases. However, some of the largest d-spacings were consistent with those of pyrrhotite, a monoclinic (FeS) compound which has hexagonal polytypes and that has been observed in high temperature quench studies (Liles and de Villiers, 2012). This composition is also different from that of the main (Fe, S) blob of experiment #9 which contains less than 2 wt.% S. These observations therefore support a quench origin for the smallest metal grains in the silicate quench.

Similar inclusions have been observed in the silicate quench of previous metal–silicate partitioning studies, carried out in both large volume experiments on sulfur partitioning (Boujibar et al., 2014) and diamond anvil cell studies of siderophile elements (Fischer et al., 2015). Boujibar et al. (2014) found that the sizes of similar grains decreased significantly at higher quench rates. Using XANES and EDX analyses, Boujibar et al. (2014) concluded that these grains, consist of FeS troilite, a different composition from that of the main coalesced metallic pool in their experiments. This

strongly argued for FeS exsolution upon quench and higher solubility of sulfur in the silicate melt at high temperatures (Boujibar et al., 2014). The sizes (50 nm), homogeneous distribution and inferred chemical composition of these grains in the silicate quench of our experiments are therefore consistent with exsolution that formed during the rapid quench.

3.3. Composition

The compositions of the quenched silicate and main metal components of the samples in this study (Table 2) were obtained from a combination of SEM-EDX, EMP-WDX analyses for major and minor elements and NanoSIMS analyses for sulfur in the silicate. After melting, the main metal blob (which had a starting composition of Fe alloyed with 3–6 wt.% S) is 70 to 90 wt.% iron and consist of 3–8 wt.% oxygen and up to 3 wt.% silicon, both of which diffused from the silicate phase during melting. The metal is also sometimes enriched in sulfur due to partitioning from the natural MORB and some sulfur heterogeneities loaded in the DAC from the Fe,S starting material. The metal of some experiments contains traces of carbon (<1 wt.%) which most likely diffused from the molten silicate or possibly from the diamond anvils during the experiments. As previously observed (e.g., Siebert et al., 2012, 2013; Fischer et al., 2015), the quenched liquid silicate is enriched in FeO by a factor of 2–3 due to preferential partitioning of FeO into the melt from the unmelted silicate (e.g., Andraut et al., 2012; Pradhan et al., 2015). Increased silicon partitioning into the metal at high temperatures could also increase the FeO content of the silicate melt through the exchange of oxygen between SiO₂ and Fe. The enrichment of FeO leads to the high oxygen fugacities in the experiments. The oxygen fugacity, expressed relative to the iron–wüstite

(IW) redox buffer, is quantified with the ratio of the activities of FeO in the molten silicate and Fe in the molten metal, assuming an ideal mixing behavior (i.e. $IW = 2\log[X_{\text{FeO}}/X_{\text{Fe}}]$). The oxygen fugacity range of these experiments is $-1.7 < \Delta IW < -1.0$. Previous sulfur partitioning experiments were carried out at oxygen fugacities that were slightly lower than or similar to the current study (Boujibar et al., 2014; Rose-Weston et al., 2009). No compositional gradients were observed in major elements in the metallic or silicate melts demonstrating that these experiments reached equilibrium. Diffusion rates of S^{2-} in silicate melts at temperature of 1400 °C (Watson, 1994) indicate that diffusive equilibration of sulfur is expected to occur in less than a minute over the typical 20 μm size of our experiments. Our experiments were carried out at much higher temperatures and under superliquidus conditions, an additional indication that equilibrium was attained.

The silicate regions of the sample can have a complicated structure and the high resolution of the NanoSIMS allows sulfur concentrations to be extracted from localized regions and from the top few atomic layers. This approach allowed a more careful characterization of the silicate than is afforded by the EMP technique which is limited in spatial resolution. Variabilities were seen in the sulfur composition from the quench silicate liquids at the sub-micron scale. Variability were sometimes due to uncoalesced metal fragments. Enrichments attributed to edge effects would also be seen around cracks and edges. We conclude that despite the experiments being fully equilibrated at high pressures and temperatures, sulfur is not homogeneously distributed in the silicate. Sulfur compositions are extracted from clean, homogeneous regions that are roughly in the middle of the melted silicate region, i.e. halfway between the edge of the metal blob and the edge of the quenched silicate. An average composition is obtained for each sample from several such regions. The partitioning coefficient was then quantified as the ratio of the average sulfur content in the metal blob and the average sulfur content in the silicate.

3.4. Parameterizing sulfur metal–silicate partitioning

Partition coefficients, which describe the distribution of an element between two immiscible phases, are functions of thermodynamic variables. Sulfur partitioning is known to vary with pressure, temperature, oxygen fugacity, silicate and metallic melt composition (Li and Agee, 2001; Rose-Weston et al., 2009; Boujibar et al., 2014). The partition coefficient of sulfur between metal and silicate D_S can be expressed as:

$$D_S = \frac{X_S^{\text{metal}}}{X_S^{\text{silicate}}} \quad (1)$$

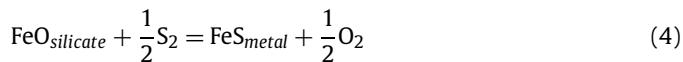
Where X_S^{metal} and X_S^{silicate} are the molar fractions of sulfur in the metal and silicate respectively. Sulfur is present as S^{2-} anions in silicate melts at oxygen fugacities relevant to core formation, below the iron–wüstite buffer (IW) (Boujibar et al., 2014). It has been proposed by Mavrogenes and O'Neill (1999) that sulfur substitutes for oxygen in silicate melts under reducing conditions following the exchange reaction:



Assuming the large majority of anions are O^{2-} , Mavrogenes and O'Neill (1999) considered the activity of O^{2-} to be constant and defined C_S the sulfide capacity which can be treated as the equilibrium constant of reaction (2):

$$C_S = X_S^{\text{silicate}} \cdot \left(\frac{f_{\text{O}_2}}{f_{\text{S}_2}} \right)^{1/2} \quad (3)$$

where f_{S_2} and f_{O_2} are the sulfur fugacity and oxygen fugacity. The equilibrium between a silicate melt and liquid metal has been previously described (e.g. Mavrogenes and O'Neill, 1999) following:



The Gibbs free energy of reaction (4) can be expressed as:

$$-\frac{\Delta_r G^0(4)}{2.303RT} = \log a_{\text{FeS}}^{\text{metal}} - \log a_{\text{FeO}}^{\text{silicate}} + \log C_S - \log X_S^{\text{silicate}} \quad (5)$$

Following Rose-Weston et al. (2009) and Boujibar et al. (2014) where $a_{\text{FeS}}^{\text{metal}}$ is approximated as the product of X_S^{metal} , molar fraction of FeS and the activity coefficient γ of FeS in the metal, sulfur partitioning is expressed by the relation:

$$\log D_S = \log a_{\text{FeO}}^{\text{silicate}} - \log \gamma_{\text{FeS}}^{\text{metal}} - \log C_S - \frac{\Delta_r G^0(4)}{2.303RT} \quad (6)$$

Since γ_{FeO} is a weak function of composition (O'Neill and Eggin, 2002), $a_{\text{FeO}}^{\text{silicate}}$ can be simply replaced by $X_{\text{FeO}}^{\text{silicate}}$ the molar fraction of FeO in the silicate melt and a constant a that also accounts for other invariable contributions. Sulfide capacity value C_S is calculated with respect to silicate melt composition following Haughton et al. (1974). At conditions of high pressure and high temperature experiments, metallic liquids can accommodate light elements other than sulfur, mainly silicon and oxygen (Siebert et al., 2012). The effect of silicon on sulfur partitioning is difficult to quantify as suitable experiments containing significant amounts of these elements simultaneously in the metal phase are scarce.

However, this effect is assumed to be negligible since above 15 GPa structures of (Fe, Si) and (Fe, S) liquids are very similar which favors ideal mixing of silicon and sulfur in Fe–S–Si ternary system (Morard and Katsura, 2010). The effect of Si on S partitioning is difficult to assess because in most previous works done in large volume experiments, S and Si were not simultaneously present in sufficient quantities in the liquid metal to allow for an estimate of a resolvable effect of silicon on sulfur partitioning (Kilburn and Wood, 1997; McCoy et al., 1999; Berthet et al., 2009). Additionally, no significant effect of sulfur on silicon partitioning has been previously reported (Siebert et al., 2004). Therefore, only one empirical term $\log(1 - X_{\text{O}})$ is added to account for the effect of oxygen on partitioning and is used as a proxy to describe activity coefficient of sulfur in the metal $\gamma_{\text{FeS}}^{\text{metal}}$. Finally, $\Delta_r G^0(4)$ can be described by pressure and temperature dependent entropy, enthalpy and volume terms, which yield the form expected for the variation in metal–silicate partitioning with pressure, temperature and composition (Boujibar et al., 2014):

$$\log [D_{m/s}(S)] = a + \frac{b}{T} + c \frac{P}{T} + \log X_{\text{FeO}}^{\text{silicate}} - \log C_S + d \log(1 - X_{\text{O}}) \quad (7)$$

Although f_{O_2} has been shown to have an effect on S partitioning (e.g. Kilburn and Wood, 1997), its partitioning as described from Eqs. (6) is independent of f_{O_2} , but by using the sulfide capacity, C_S the effect of f_{O_2} can be extracted. Under reducing conditions (below IW-3) sulfur partitioning strongly decreases and sulfur even behaves as a lithophile element below IW-4 (Kilburn and Wood, 1997; Rose-Weston et al., 2009); while under more oxidizing conditions between IW-1 and IW-3, covering the range of f_{O_2} of this work, partitioning likely remains constant (Rose-Weston et al., 2009). The effect of f_{O_2} on partitioning is captured by the model (i.e. Eqs. (7)) through compositional changes with f_{O_2} represented by the FeO content of the silicate melt $X_{\text{FeO}}^{\text{silicate}}$ and the sulfide capacity C_S (Rose-Weston et al., 2009).

The measured partitioning coefficients of sulfur in this study range from 8 to 55, (Table 1). No difference was observed in

Table 1

Experimental summary of the sulfur partitioning experiments. $D_{m/s}$ = metal–silicate partitioning coefficients, calculated from NanoSIMS measurements of sulfur in the silicate (except for run #3 which was measured by EMP); quantities used in the calculation are in moles. ΔIW = oxygen fugacity, calculated relative to the iron–wüstite (IW) redox buffer. X = molar fractions. † KLB-1 starting silicate composition, unmarked MORB starting silicate.

Run #	Pressure (GPa)	Temperature (K)	$D_{m/s}$	ΔIW	$X_{FeO_{sil}}$	$X_{Fe_{met}}$	$X_{S_{met}}$	$X_{O_{met}}$	$X_{Si_{met}}$
†1	46	3100	20.94 ± 3.75	−1.66	0.10	0.70	0.13	0.11	0.03
2	52	3700	13.59 ± 3.27	−1.30	0.14	0.61	0.15	0.19	0.03
†3	58	3600	10.34 ± 1.24	−1.45	0.13	0.70	0.07	0.14	0.06
4	59	3500	22.12 ± 3.96	−1.08	0.21	0.73	0.12	0.13	0.01
5	60	3300	54.47 ± 4.22	−1.31	0.17	0.78	0.07	0.13	0.04
6	66	3600	13.60 ± 1.94	−1.00	0.17	0.55	0.16	0.21	0.05
7	74	3700	17.04 ± 2.01	−1.06	0.02	0.68	0.14	0.14	0.02
8	85	4000	15.30 ± 2.12	−1.47	0.14	0.74	0.04	0.17	0.04
9	91	4100	7.96 ± 1.83	−1.55	0.12	0.71	0.03	0.17	0.06

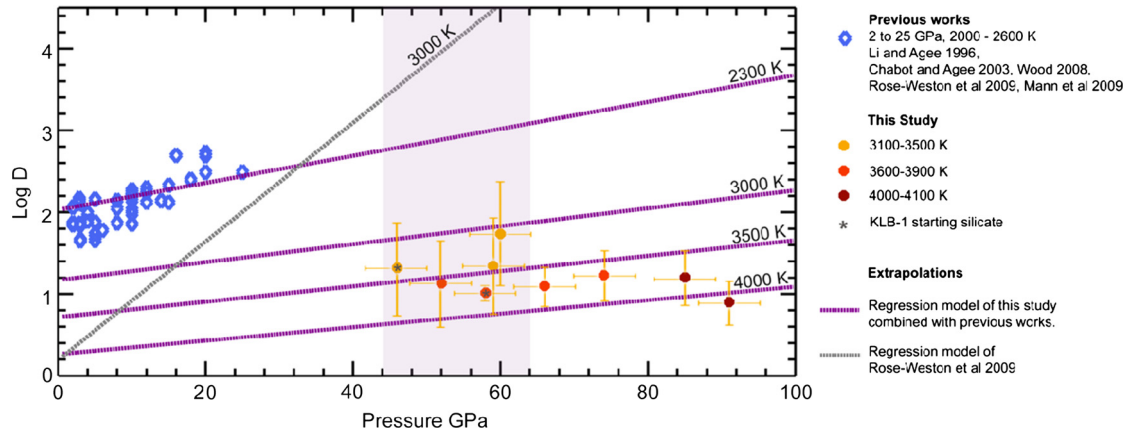


Fig. 6. Partition coefficient as a function of pressure showing data from this study (dots), previous studies (diamonds) and the temperature dependent extrapolations from multivariable regression of the combined data set. Parameters used are: $\log C_S = -5.372$ (calculated for a primitive pyrolite mantle composition), $X_{FeO} = 0.057$ (mole fractions of FeO in the mantle, Siebert et al., 2013) and X_O evolving from 0.02 to 0.12 mole fractions (O content of the growing core during Earth accretion). The extrapolation of Rose-Weston et al. (2009) for 3000 K is also shown. The shaded region is the pressure range of core–mantle equilibration proposed by previous works (e.g., Siebert et al., 2012).

the partitioning results between the two different starting silicate composition. The results of this study were combined with results from previous works (Wood, 2008; Rose-Weston et al., 2009; Mann et al., 2009; Chabot and Agee, 2003; Li and Agee, 1996) in order to obtain constants a , b , c , d from least square multivariable regression of the model shown in Eqs. (7). The results of Boujibar et al. (2014) are not included due to the high carbon content of the quench metal in those experiments. A single regression provides an adequate fit to the full set of selected data, including pressures from 1 to 91 GPa and temperatures from 1873 to 4100 K, with the relation:

$$\log D_S = -3.30(\pm 0.47) + \frac{3000(\pm 1023)}{T} + 33(\pm 11) \frac{P}{T} + \ln X_{FeO}^{silicate} - \ln C_S + 14(\pm 2) \ln(1 - X_O) \quad (8)$$

Fig. 6 reports sulfur partitioning results from a combined dataset, interpolations using the model (Eqs. (8)) and predictions from the model of (Rose-Weston et al., 2009). The regressions constants from this study and two previous studies are shown in Table 3. As with previous works (Li and Agee, 2001; Rose-Weston et al., 2009; Boujibar et al., 2014) both b and c are positive indicating an increasing siderophile behavior with increasing pressure and decreasing siderophile behavior with increasing temperature. The constant b which is related to the enthalpy change of reaction (4) and effect of temperature is smaller than that of Rose-Weston et al. (2009) and larger than that of Boujibar et al. (2014). The constant c which is related to the volume change of reaction (4), is smaller than that obtained in those two previous works. This shows that

pressure effect on sulfur partitioning has been previously over estimated using data from a smaller P – T range than this work. Finally, the d constant which is related to the oxygen content of the metal is about a factor of two less than the value obtained by Boujibar et al. (2014). This difference may be explained by the regression of a dataset with a smaller range of oxygen contents in the metal (below 0.5 wt.%) than in the present work where much higher temperatures enhance oxygen solubility in metal (up to 8 wt.%). Previous works (Rose-Weston et al., 2009; Boujibar et al., 2014) predicted that sulfur partitioning would increase strongly at higher pressures and decrease at higher temperatures. Rose-Weston et al. (2009) predicted sulfur partitioning to be above 5000 at pressures of 50 GPa and 3000 K, two orders of magnitude higher than the values that were directly measured in our study. Following from our results, temperature is the dominant effect on sulfur partitioning.

4. Discussion

4.1. Single stage core formation

Analyses of upper mantle samples yield a bulk silicate Earth with 200 ± 80 ppm of sulfur (e.g. McDonough and Sun, 1995; Lorand and Alard, 2010; Wang and Becker, 2013; Lorand et al., 2013). This estimate and a volatile depleted-carbonaceous chondrites (CI) composition for the bulk earth, gives a value of core–mantle sulfur distribution, $D_S \sim 100 \pm 30$ (e.g. Wang and Becker, 2013). If the record of core formation is preserved in the mantle then similar values of metal–silicate partitioning for sulfur are required. The

Table 2

Silicate and metallic composition in weight % of run products. Measured by EDX, † EPM and ★ NanoSIMS. Minor elements included in total.

	Run #								
	1	2	3	4	5	6	7	8	9
Pressure (GPa)	46	52	58	59	60	66	74	85	91
Temperature (K)	3100	3700	3600	3500	3300	3600	3700	4000	4100
Silicate composition									
MgO	† 32.35 ± 0.53	8.46 ± 0.10	† 33.32 ± 0.28	6.52 ± 0.05	5.48 ± 0.15	6.36 ± 0.04	6.34 ± 0.01	8.96 ± 0.11	8.64 ± 0.47
SiO ₂	† 41.40 ± 0.48	40.83 ± 0.03	† 39.67 ± 0.84	38.75 ± 0.13	38.99 ± 0.70	36.0 ± 0.27	36.23 ± 0.19	32.23 ± 0.71	35.58 ± 0.73
Al ₂ O ₃	† 4.88 ± 0.13	18.07 ± 0.15	† 4.99 ± 0.11	16.59 ± 0.11	21.19 ± 0.53	18.86 ± 0.11	19.21 ± 0.14	22.30 ± 0.01	28.64 ± 1.17
CaO	† 4.66 ± 0.056	6.14 ± 0.04	† 3.77 ± 0.078	3.75 ± 0.003	3.77 ± 0.20	3.54 ± 0.134	3.09 ± 0.02	3.26 ± 0.1	3.53 ± 0.15
Na ₂ O	† 0.14 ± 0.026	4.09 ± 0.20	–	3.82 ± 0.05	3.52 ± 0.07	3.82 ± 0.08	4.29 ± 0.13	7.21 ± 0.67	3.25 ± 0.39
K ₂ O	–	1.2 ± 0.12	–	1.34 ± 0.03	1.75 ± 0.01	2.13 ± 0.05	1.3 ± 0.05	1.63 ± 0.10	0.77 ± 0.08
FeO	† 17.69 ± 0.26	32.37 ± 0.23	† 18.06 ± 0.73	24.50 ± 0.2	21.82 ± 1.05	22.0 ± 0.19	25.62 ± 0.28	17.87 ± 0.56	15.55 ± 2.48
CoO	† 0.04 ± 0.03	–	† 0.11 ± 0.02	–	–	–	–	–	–
TiO ₂	–	2.87 ± 0.04	–	2.45 ± 0.015	3.27 ± 0.05	4.68 ± 0.13	2.47 ± 0.02	3.47 ± 0.14	3.96 ± 0.23
MoO ₂	† 0.14 ± 0.11	–	0.19 ± 0.02	–	–	–	–	–	–
WO ₃	† 0.80 ± 0.049	–	† 0.174 ± 0.118	–	–	–	–	–	–
S	★ 0.3801 ± 0.0680 † 0.1884 ± 0.290	★ 0.7714 ± 0.1410	★ 0.4270 ± 0.051 † 0.2030 ± 0.3100	★ 0.2967 ± 0.5300	★ 0.07421 ± 0.0056	★ 0.6728 ± 0.079	★ 0.6367 ± 0.012	★ 0.1358 ± 0.158 † 0.1478 ± 0.652	★ 0.2120 ± 0.0472
Total	98.43	100.4	101.465	100.2	99.89	99.4	99.98	97.74	100.32
Metal composition									
O	† 3.40 ± 0.07	6.39 ± 1.25	† 4.15 ± 0.27	4.36 ± 0.10	3.81 ± 0.09	7.86 ± 2.00	4.75 ± 1.70	5.82 ± 0.47	5.84 ± 1.63
Fe	† 76.94 ± 0.36	69.64 ± 3.38	† 74.74 ± 0.57	85.98 ± 0.06	89.18 ± 0.10	72.0 ± 2.73	81.67 ± 3.9	87.86 ± 0.49	83.97 ± 3.27
Si	† 1.50 ± 0.03	1.74 ± 0.67	† 2.96 ± 0.16	2.03 ± 0.05	0.68 ± 0.01	2.96 ± 0.02	1.29 ± 0.24	2.11 ± 0.14	3.38 ± 0.90
Mn	–	–	–	–	–	–	0.28 ± 0.01	–	1.05 ± 0.08
Al	† 0.02 ± 0.01	0.28 ± 0.21	† 0.04 ± 0.01	0.28 ± 0.06	0.06 ± 0.015	1.71 ± 0.18	–	0.77 ± 0.07	0.99 ± 0.29
Mg	† 0.12 ± 0.008	0.22 ± 0.18	† 0.25 ± 0.02	–	–	0.44 ± 0.06	0.28 ± 0.06	–	0.35 ± 0.09
Mo	† 3.46 ± 0.14	–	† 3.49 ± 0.14	–	–	–	–	–	–
W	† 1.81 ± 0.21	–	† 2.25 ± 0.16	–	–	–	–	–	–
S	† 8.35 ± 0.06	10.00 ± 0.34	† 4.43 ± 0.08	7.89 ± 0.03	4.71 ± 0.015	12.28 ± 0.18	9.32 ± 0.19	2.53 ± 0.16	1.96 ± 0.02
Total	96.17	99.41	93.46	100	99.79	97.58	98.32	99.85	97.55

Table 3

Regression parameters from this study, Rose-Weston et al. (2009) and Boujibar et al. (2014).

Study	<i>a</i> (intercept)	<i>b</i> (1/ <i>T</i>)	<i>c</i> (<i>P/T</i>)	<i>d</i> (log(1 − <i>X</i> ₀))
This work	−3.50 ± 0.47	3000 ± 1023	33 ± 11	14 ± 2
Rose-Weston et al. (2009)	−4.37	13686	217.49	–
Boujibar et al. (2014)	−3.72 ± 0.07	405 ± 150	136 ± 25	31.4 ± 18

addition of $\sim 0.5 \pm 0.2\%$ Earth mass of volatile rich late accretion (of CI composition) after core formation, has also been proposed to account for a large fraction of the budget of sulfur in the present mantle (Rose-Weston et al., 2009). Using the new results for sulfur partitioning combined with a core formation model, new constraints are provided on (1) the amount of sulfur in the core, (2) the proportion of late accreted sulfur in the mantle, and (3) the relative timing for the delivery of moderately volatile elements such as sulfur to the Earth.

Our experimental results show that sulfur is less siderophile than expected from previous works (Li and Agee, 2001; Rose-Weston et al., 2009; Boujibar et al., 2014) at the putative conditions of the base of the magma-ocean ($\sim 55 \pm 10$ GPa; $\sim 3500 \pm 500$ K; (Siebert et al., 2012, 2013; Fischer et al., 2015). These results imply that a single stage core formation event (Stevenson, 1990) occurring between 45 and 65 GPa and 3500 and 4000 K (mantle liquidus from the mean of Fiquet et al. (2010) and Andraut et al. (2011)) at the present-day oxygen fugacity of core-mantle equilibrium (IW-2.3; $X_{\text{FeO}} = 0.057$; $X_{\text{Fe}} = 0.8$) could not generate a core containing more than ~ 1.2 wt.% sulfur to account for a maximum of 280 ppm sulfur in the mantle; A low upper bound value considering previous geochemical estimates of sulfur in the core of approximately 2 wt.% (e.g. McDonough, 2003). However, single stage core formation models do not integrate the disparity of P – T – f_{O_2} – X conditions of equilibration over the course of accretion.

4.2. Multi-stage core formation model

Continuous or multistage core formation (Wade and Wood, 2005; Rubie et al., 2011) in which P – T – X conditions at the base of the magma ocean, the locus of final core–mantle equilibrium, change with time as the Earth grows has been proposed as a more physically plausible process. The parameterization of sulfur partitioning obtained in this study were used to determine the behavior of sulfur in a similar scenario. In the present model, the Earth accretes mass according to a linear growth function. The sizes of the impactors were varied in order to investigate the effects of the delivery of sulfur by bodies with a range of masses. The first $\sim 80\%$ of Earth's mass is delivered by small planetary bodies of $\sim 0.1\%$ Earth mass. The final $\sim 20\%$ of the Earth's mass is added by several embryos of 3 to 4% Earth mass followed by a larger body of 10% the Earth mass, the approximate size of the proposed last giant impactor (e.g., Canup, 2012). The impactors are assumed to have been already differentiated into silicate mantles and metallic cores with similar core mantle fractions as the Earth (i.e. 68 wt.% mantle and 32 wt.% core). Minor amounts of chondritic material, 0.5% Earth mass is added (as a single body) following the cessation of core formation to evaluate the effect of a late veneer (e.g., Walker, 2009) on the sulfur abundance in the silicate Earth.

At each step of accretion, the metal and silicate equilibrate at the base of the magma ocean fixed at 40% of the growing Earth's core–mantle boundary pressure (Siebert et al., 2012) and at the temperature of the pyrolite liquidus at that pressure (Fiquet et al., 2010; Andraut et al., 2011). Evolution equations for the concentrations of sulfur in the core and sulfur in the mantle are derived from mass balance considerations in the accreting Earth following the approach of Rudge et al. (2010) and Deguen et al. (2014), Eqs. (9) and (10). This approach allows the investigation of the

effect of partial equilibration of impactor cores with the Earth's mantle, for large differentiated embryos (e.g. Dahl and Stevenson, 2010; Deguen et al., 2014). Complete equilibration is assumed during the accretion of the first 80% of the Earth as emulsification of metallic cores from the small bodies into ~ 1 cm size droplets allow full metal–silicate equilibrium (Rubie et al., 2003). Partial equilibration is included in the model only during the addition of the final larger bodies as complete emulsification of large cores is unlikely. Only a fraction of the large impactor cores re-equilibrates with the Earth's mantle while the remaining fraction is added directly to the Earth's core. From Deguen et al. (2014), the evolution of the sulfur concentration of the Earth's core and mantle are:

$$\frac{d}{dt}(Mc_m) = [\mathcal{E}_i D_i c_s + (1 - \mathcal{E}_i) c_m^{imp}] \frac{dM}{dt} \quad (9)$$

$$\frac{d}{dt}(Mc_s) = \left[c_s^{imp} + \mathcal{E}_i \frac{F}{1-F} (c_m^{imp} - D_i c_s) \right] \frac{dM}{dt} \quad (10)$$

where M is the mass fraction of the Earth; c_m and c_m^{imp} are the concentrations of sulfur in the Earth's and impactor's core respectively; c_s and c_s^{imp} are the concentrations of sulfur in the Earth's and impactor's mantle respectively; F represents the mass fraction of metal (the same as Earth's current core mass fraction $F = 0.32$); D_i is the metal–silicate partitioning for sulfur calculated from Eq. (8). The evolution of sulfur concentration in core and metal also depends on the quantity of silicates that equilibrates with the metal. According to hydrodynamic model from (Deguen et al., 2014), a parameter for the equilibrium efficiency of sulfur \mathcal{E}_i is defined to express the mass exchange between the segregating core and mantle normalized by the maximum possible mass exchange:

$$\mathcal{E}_i = \frac{k}{1 + \frac{D_i}{\Delta}} \quad (11)$$

where k is the fraction of the impactor core that re-equilibrates with the Earth's mantle, assumed to be 1 in the modeling; Δ the ratio of equilibrated silicate to equilibrated metal (dilution ratio) can be expressed at each step of accretion following Deguen et al. (2014) as:

$$\Delta = \frac{\rho_{\text{silicate}}}{\rho_{\text{metal}}} \left[\left[1 + \frac{0.25}{\delta^{1/3}} \right]^3 - 1 \right] \quad (12)$$

in which ρ_{silicate} and ρ_{metal} are the densities of silicate and metal respectively, and δ is the ratio of the impactor mass to Earth's mass.

The stage of growth at which sulfur was added to the Earth can have strong implications for the distribution of sulfur in the core and mantle. Two different accretionary scenarios were considered. In the first referred as the homogeneous scenario, sulfur is added continuously by impactors containing a bulk sulfur content similar to that estimated for the Earth of 6400 ppm (McDonough, 2003). In the second case referred as the heterogeneous scenario, sulfur is added only in the last 20% of accretion by larger planetary embryos containing a bulk sulfur content of ~ 2.5 wt.% in order to obtain the bulk Earth sulfur content of 6400 ppm at the end of accretion.

Results of the modeling are reported in Fig. 7. The homogeneous case yields higher sulfur content than the observed bulk silicate Earth values. The mantle sulfur concentration quickly reaches

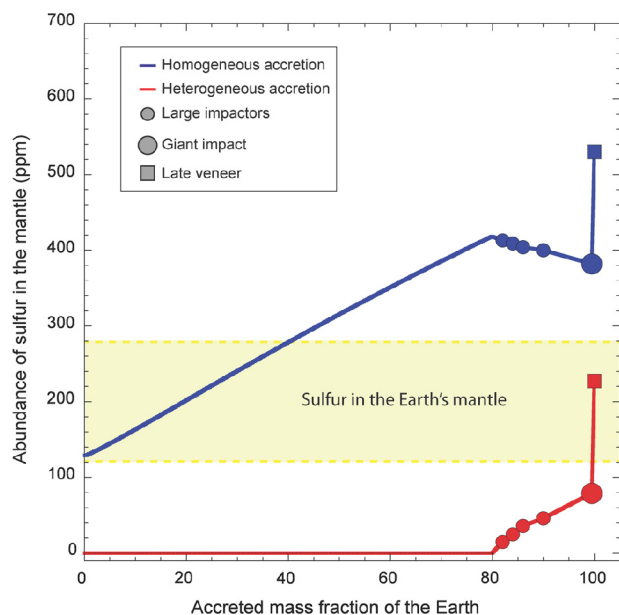


Fig. 7. Sulfur accreted to the mantle for two accretionary scenarios, homogeneous and heterogeneous accretion. In the homogeneous case bodies contain the same amount of sulfur throughout accretion. During heterogeneous accretion sulfur is only added after the Earth has accreted to ~ 0.8 of its mass fraction and bodies richer in S are added.

a high value (above 400 ppm) as the high temperatures in the deep magma ocean allows for efficient re-equilibration of the small cores of accreting bodies with the mantle (\mathcal{E}_S up to around 0.3). Strong decrease of sulfur partitioning at the high temperature of the base of the deepening magma ocean quickly drives the sulfur mantle content toward a value around 450 ppm. The sulfur content of the mantle drops to slightly lower values during the last 20% of accretion as equilibrium efficiency is significantly reduced for large impacts where impactor core diameters approach the magma ocean depth (Deguen et al., 2014). A final core composition of ~ 1.9 wt.% is obtained in this scenario. Finally, a late veneer consisting of 0.5% Earth mass (Walker, 2009) and average CI composition is added to obtain a final mantle sulfur budget slightly above 500 ppm, at least two times more than the observed sulfur content of the mantle. As moderately siderophile elements such as Ni and Co require that a significant fraction of metal must have undergone re-equilibration with the mantle (Rudge et al., 2010), our results rule out the possibility of continuous accretion of volatile elements such as sulfur during the process of accretion and core formation of the Earth. Additionally, for any considered oxygen fugacity variation during accretion, either starting from highly reduced components (Wood and Halliday, 2005) or oxidized components (Siebert et al., 2013), a model (with continuous addition of sulfur) leading to the 200 ± 80 ppm sulfur in the present-day Earth's mantle was not obtained. In agreement with the conclusion raised for the single stage core formation model, only a bulk Earth containing lower amounts of sulfur could account for the observed mantle composition. However, this seems at odds with lower bound cosmochemical estimates of bulk Earth sulfur content (e.g., McDonough and Sun, 1995; Allègre et al., 2001). Such change in the bulk Earth sulfur content would imply that the order of element volatility calculated for solar nebula condensation is not applicable to planetary composition which is a controversial issue (Wang et al., 2016).

Overenrichment of sulfur in the mantle has been reported in recent work by Rubie et al. (2016) using *N*-body accretion simulations. Strong decrease of sulfur solubility in silicate melt with decreasing temperature at high pressure has been predicted by

Laurenz et al. (2016). Exsolution of FeS from the magma ocean upon cooling at high pressure and segregation by sinking to the core is proposed as a potential mechanism to reduce the mantle's sulfur content (Rubie et al., 2016). The present dataset does not report sulfide saturation experiments and is not directly applicable for estimating sulfur solubility at *HP-HT*. However, sulfur partitioning between FeS and silicate predicted from sulfide saturation experiments at *P-T* conditions of the magma ocean (Laurenz et al., 2016) is at least an order of magnitude higher than sulfur metal-silicate partitioning obtained directly at these conditions from our work. The very strong negative pressure effect on sulfur solubility reported by Laurenz et al. (2016) likely explains such discrepancy. Additionally, a correction for sulfur activity in metal is missing, which would be necessary for a proper comparison of this work and solubility measurements. FeS saturation experiments at direct conditions of the bottom of the magma ocean are required to precisely quantify the relevance of such mechanism to strip the excess sulfur of the mantle to the core.

In contrast with the homogeneous case, heterogeneous accretion can match the observed mantle sulfur content of 200 ± 80 ppm (Fig. 7). Late addition of sulfur in the last 20% of accretion from large planetary embryos (from 3 to 10% of Earth's mass) implies much lower re-equilibration efficiency of the metal which results in more sulfur being added to the core (1.94 wt.%). This scenario allows for a bulk Earth sulfur content of $\sim 6000 \pm 1000$ ppm as implied by the volatility trend of elements in the Earth (e.g., McDonough and Sun, 1995; Allègre et al., 2001). However, core formation model involving higher mass fraction of silicate mantle that re-equilibrates with accreted metal than the present model (from 3 to 10% for the final impacts) would lead to an excess of sulfur in the mantle. The heterogeneous scenario including late volatile addition and sulfur-rich iron liquid segregation to the core, often referred as the Hadean Matte, has been invoked to explain numerous observations: (1) a low density layer at the top of the core (e.g., Helffrich and Kaneshima, 2013); (2) the mismatch of various core formation chronometers (Wood and Halliday, 2005); (3) the abundance of moderately siderophile elements such as W and Mo and the C/S ratio in the mantle (Wade et al., 2012; Li et al., 2016); (4) the suprachondritic Ru/Ir and Pd/Ir ratios in the Earth's mantle (Laurenz et al., 2016); (5) *N*-body simulations showing late accretion of materials derived from further out in the solar system (Raymond et al., 2006; Morbidelli et al., 2012) or (6) isotopic composition of the bulk silicate Earth and chondrites in Ag or Cu (Schönbächler et al., 2010; Savage et al., 2015). If the ability of incomplete equilibration to produce the above mentioned geochemical signatures needs to be explored, the heterogeneous model is compatible with a major fraction of the sulfur in the mantle being inherited from core-mantle differentiation as was proposed to explain sulfur isotopic composition of the BSE (Labidi et al., 2013).

5. Conclusion

Laser heated diamond anvil cell experiments have been performed to study the metal-silicate partitioning behavior of sulfur at pressures and temperatures relevant to core formation in a deep magma ocean (above 40 GPa and 3500 K). Sulfur is less siderophile than predicted by thermodynamic extrapolations from lower *P-T* experiments (Rose-Weston et al., 2009; Boujibar et al., 2014). Application of our partitioning results to a single stage core formation model shows that Earth's core cannot contain more than 1.2 wt.% sulfur to account for the present sulfur content of the mantle. More complete modeling including changes in *P-T-X-f_{O2}* conditions during the Earth's growth, partial equilibration of both metal and silicate and the relative timing of sulfur delivery during accretion have been performed. A model of continuous delivery of

volatiles yields an excess of sulfur in the mantle and could only be reconciled with a lower bulk Earth and core sulfur content (~ 3000 ppm and ~ 1 wt.% respectively) than proposed from geochemical estimates ($\sim 6000 \pm 1000$ ppm and 2 wt.%). Late addition of sulfur during the last 20% of Earth accretion from large differentiated planetary embryos provides a possible mechanism to obtain 2 wt.% sulfur in the core and to match the observed sulfur content of the mantle due to significantly lowered metal–silicate equilibrium efficiency. The potential presence of volatiles as core formation proceeds requires low degree of core–mantle equilibration to explain the mantle abundance of these elements. This implies that a major fraction of sulfur in the present mantle records the imprint of core–mantle equilibrium.

For any accretion and core formation scenarios, the low metal–silicate partitioning values of sulfur at P – T conditions of the magma ocean base rule out sulfur as a major light element in the Earth's core (i.e. there is less than 2 wt.% sulfur in the core). In contrast with recent works (O'Brien et al., 2014; Rubie et al., 2016), we argue that sulfur and by analogy other volatiles were not accreted continuously during Earth's accretion. Models favoring later addition of volatiles and sulfur, either during the last 10–20% of accretion similar to our heterogeneous model (e.g., O'Neill, 1991; Wade et al., 2012; Wohlers and Wood, 2015; Albarede et al., 2013), or by the late veneer only (Albarede, 2009; Wang and Becker, 2013) are promoted.

Acknowledgements

This work was supported by French state funds managed by ANR within the Investissements d'Avenir program under reference ANR-11-IDEX-0004-02, and more specifically within the framework of the Cluster of Excellence MATISSE led by Sorbonne Universités. J.S. acknowledges support from the French National Research Agency (ANR project VolTerre, grant no. ANR-14-CE33-0017-01). The authors are grateful for the use of the National NanoSIMS facility at the MNHN which was established by funds from the CNRS, Region Île de France, Ministère délégué à l'Enseignement supérieur et à la Recherche. We are also grateful for the use of the FIB/MEB platforms at IPGP and IMPMC and the EMP at CAMPParis. The authors acknowledge Stephan Borensztajn's and Iméne Esteve's FIB preparation work, Gilles Le Marchand for help with sample recovery, Adriana Gonzalez for providing assistance with the NanoSIMS measurements, Guillaume Morard for providing starting materials and Michele Fialin for help with sample characterization. T.-A.S. acknowledges communication with John Rudge. We thank J. Brodholt for editorial handling and two anonymous reviewers for their constructive comments that improved the manuscript.

Appendix A. Starting materials

Starting Fe,S alloys were synthesized by either the planar flow casting technique (Morard et al., 2011) or by low pressure metal–

Table A.4

Major oxide composition in weight% of starting silicate peridotite (KLB1) and MORB as quantified by EMP. Minor elements included in total.

Oxides	KLB-1	MORB
SiO ₂	43.06 ± 0.20	49.74 ± 0.49
FeO	7.44 ± 0.18	9.73 ± 0.28
MgO	37.10 ± 0.22	8.46 ± 0.12
Al ₂ O ₃	3.53 ± 0.04	15.89 ± 0.23
CaO	3.55 ± 0.06	11.74 ± 0.19
Na ₂ O	0.02 ± 0.01	2.69 ± 0.09
TiO ₂	1.08 ± 0.06	1.33 ± 0.13
MnO	1.08 ± 0.06	0.18 ± 0.06
Total	97.32	100.1

silicate partitioning experiments done in a piston cylinder at superliquidus conditions (in which case a 1 mm diameter (Fe,S) alloy was manually separated from the silicate in the quenched run product).

Appendix B. NanoSIMS measurements and calibration

A large area of each samples was pre-sputtered for up to 10 min with a high primary current in order to implant Cs⁺ ions into the sample matrix (Hoppe et al., 2013). A 10 pA primary current of Cs⁺ accelerated at 16 keV with a spot size of 300 nm was then used for the analysis. During the analysis, the beam was rastered over a square region which ranged from 8×8 to 20×20 μm . These areas corresponded to images that were 256×256 pixels. Integration times ranged from 30 min to 90 min during which several tens of data frames (up to 60), which recorded accumulated counts, were collected. The data frames were deadtime-corrected and aligned to produce a map of the total counts over all cycles, for each specie.

Ratio maps (e.g. sulfur/silicon) were then produced. Converting the NanoSIMS measurements from ratio of sulfur/silicon counts to sulfur composition relied on the linear dynamic range of the NanoSIMS and standard calibrations carried out during each session. Several glass standards with known sulfur and silicon compositions were used during each NanoSIMS session: NIST610 (Sylvester and Eggins, 1997), 456 ppm, CLDR01-5V (Chaussidon et al., 1991) 950 ppm, NMORB-blank1, internally synthesized, measured by EMP, containing 0 to 10 ppm (Table B.5). The sulfur/silicon measurements obtained for the DAC thin sections were then compared to those obtained for the standards (see sulfur calibration curve Fig. B.8). Sulfur concentration in the DAC samples were obtained by inverse regression following the method of Thomen et al. (2014).

Table B.5

³²S/²⁸Si ratios for the NanoSIMS standards that were used to convert the measured ³²S/²⁸Si ratios of samples to sulfur concentrations.

Standard name	³² S/ ²⁸ Si	S ppm
CLDR1-05V	4.88E–02	950
NBS 610	2.33E–02	456
NBS 612	1.13E–02	200
NMORB-blank1	6.79E–05	12

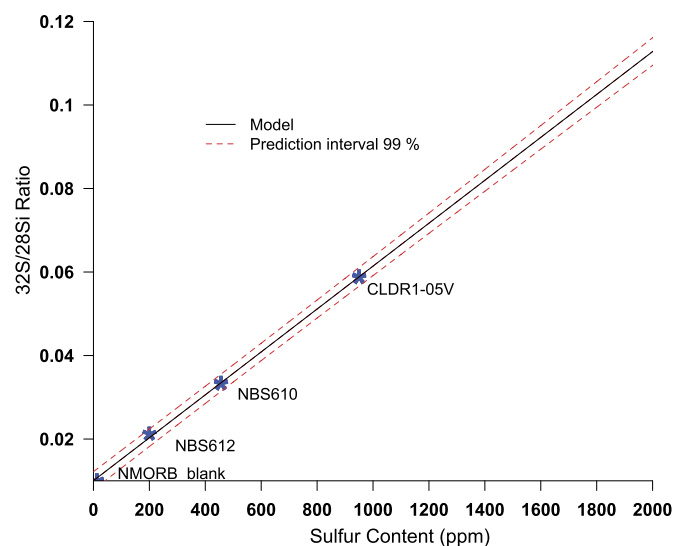


Fig. B.8. NanoSIMS calibration curve for sulfur analysis from one session. Y axis shows ³²S/²⁸S ratios measured by the NanoSIMS in each standard while the x axis shows the sulfur abundances in ppm, independently determined by LA-ICPMS.

References

- Ahrens, T.J., 1979. Equation of state of iron sulfides and constraints on the sulfur content of the Earth. *Geophys. Res. Lett.* 11, 130–134.
- Albarede, F., 2009. Volatile accretion history of the terrestrial planets and dynamic implications. *Nature* 461 (7268), 1227–1233.
- Albarede, F., Ballhaus, C., Blichert-Toft, J., Lee, C.-T., Marty, B., Moynier, F., Yin, Q.-Z., 2013. Asteroidal impacts and the origin of terrestrial and lunar volatiles. *Icarus* 222 (1), 44–52.
- Alfe, D., Gillan, M.J., Price, G.D., 2000. Constraints on the composition of the Earth's core from ab initio calculations. *Nature* 405 (6783), 172–175.
- Allègre, C., Manhès, G., Lewin, É., 2001. Chemical composition of the earth and the volatility control on planetary genetics. *Earth Planet. Sci. Lett.* 185 (1), 49–69.
- Andraut, D., Bolfan-Casanova, N., Nigro, G.L., Bouhifd, M.A., Garbarino, G., Mezouar, M., 2011. Solidus and liquidus profiles of chondritic mantle: implication for melting of the Earth across its history. *Earth Planet. Sci. Lett.* 304 (1–2), 251–259. <http://dx.doi.org/10.1016/j.epsl.2011.02.006>.
- Andraut, D., Petitgirard, S., Nigro, G.L., Devidal, J.-L., Veronesi, G., Garbarino, G., Mezouar, M., 2012. Solid-liquid iron partitioning in Earth's deep mantle. *Nature* 487 (7407), 354–357.
- Badro, J., Côté, A.S., Brodholt, J.P., 2014. A seismologically consistent compositional model of Earth's core. *Proc. Natl. Acad. Sci. USA* 111 (21), 7542–7545. <http://dx.doi.org/10.1073/pnas.1316708111>.
- Berthet, S., Malavergne, V., Righter, K., 2009. Melting of the indarch meteorite (EH4 chondrite) at 1 GPa and variable oxygen fugacity: implications for early planetary differentiation processes. *Geochim. Cosmochim. Acta* 73 (20), 6402–6420.
- Boehler, R., 2000. High-pressure experiments and the phase diagram of lower mantle and core materials. *Rev. Geophys.* 38 (2), 221–245. <http://dx.doi.org/10.1029/1998RG000053>.
- Boujibar, A., Andraut, D., Bouhifd, M.A., Bolfan-Casanova, N., Devidal, J.-L., Trcera, N., 2014. Metal-silicate partitioning of sulphur, new experimental and thermodynamic constraints on planetary accretion. *Earth Planet. Sci. Lett.* 391, 42–54. <http://dx.doi.org/10.1016/j.epsl.2014.01.021>.
- Canup, R.M., 2012. Forming a Moon with an Earth-like composition via a giant impact. *Science* 338 (6110), 1052–1055. <http://dx.doi.org/10.1126/science.1226073>.
- Chabot, N.L., Agee, C.B., 2003. Core formation in the Earth and Moon: new experimental constraints from V, Cr, and Mn. *Geochim. Cosmochim. Acta* 67 (11), 2077–2091. [http://dx.doi.org/10.1016/S0016-7037\(02\)01272-3](http://dx.doi.org/10.1016/S0016-7037(02)01272-3).
- Chaussidon, M., Sheppard, S.M., Michard, A., 1991. Hydrogen, sulphur and neodymium isotope variations in the mantle beneath the EPR at 12°50'N. *Stable Isot. Geochim. Tribute to Samuel Epstein* 7 (3), 325.
- Dahl, T.W., Stevenson, D.J., 2010. Turbulent mixing of metal and silicate during planet accretion and interpretation of the Hf–W chronometer. *Earth Planet. Sci. Lett.* 295 (1–2), 177–186. <http://dx.doi.org/10.1016/j.epsl.2010.03.038>.
- Deguen, R., Landeau, M., Olson, P., 2014. Turbulent metal-silicate mixing, fragmentation, and equilibration in magma oceans. *Earth Planet. Sci. Lett.* 391, 274–287. <http://dx.doi.org/10.1016/j.epsl.2014.02.007>.
- Fiquet, G., Auzende, A.L., Siebert, J., Corgne, A., Bureau, H., Ozawa, H., Garbarino, G., 2010. Melting of peridotite to 140 gigapascals. *Science* 329 (5998), 1516–1518. <http://dx.doi.org/10.1126/science.1192448>.
- Fischer, R.A., et al., 2015. High pressure metal-silicate partitioning of Ni, Co, V, Cr, Si, and O. *Geochim. Cosmochim. Acta* 167, 177–194. <http://dx.doi.org/10.1016/j.gca.2015.06.026>.
- Halliday, A.N., 2013. The origins of volatiles in the terrestrial planets. *Geochim. Cosmochim. Acta* 105, 146–171. <http://dx.doi.org/10.1016/j.gca.2012.11.015>.
- Haughton, D.R., Roeder, P.L., Skinner, B.J., 1974. Solubility of sulfur in mafic magmas. *Econ. Geol.* 69 (4), 451–467. <http://dx.doi.org/10.2113/gsecongeo.69.4.451>.
- Helffrich, G., Kaneshima, S., 2013. Causes and consequences of outer core stratification. *Phys. Earth Planet. Inter.* 223, 2–7.
- Hoppe, P., Cohen, S., Meibom, A., 2013. NanoSIMS: technical aspects and applications in cosmochemistry and biological geochemistry. *Geostand. Geanal. Res.* 37 (2), 111–154. <http://dx.doi.org/10.1111/j.1751-908X.2013.00239.x>.
- Kilburn, M., Wood, B., 1997. Metal-silicate partitioning and the incompatibility of S and Si during core formation. *Earth Planet. Sci. Lett.* 152 (1–4), 139–148. [http://dx.doi.org/10.1016/S0012-821X\(97\)00125-8](http://dx.doi.org/10.1016/S0012-821X(97)00125-8).
- Labidi, J., Cartigny, P., Moreira, M., 2013. Non-chondritic sulphur isotope composition of the terrestrial mantle. *Nature* 501 (7466), 208–211.
- Laurenz, V., Rubie, D.C., Frost, D.J., Vogel, A.K., 2016. The importance of sulfur for the behavior of highly-siderophile elements during Earth's differentiation. *Geochim. Cosmochim. Acta* 194, 123–138.
- Li, J., Agee, C.B., 1996. Geochemistry of mantle-core differentiation at high pressure. *Nature* 381 (6584), 686–689.
- Li, J., Agee, C.B., 2001. Element partitioning constraints on the light element composition of the Earth's core. *Geophys. Res. Lett.* 28 (1), 81–84. <http://dx.doi.org/10.1029/2000GL012114>.
- Li, Y., Dasgupta, R., Tsuno, K., Monteleone, B., Shimizu, N., 2016. Carbon and sulfur budget of the silicate Earth explained by accretion of differentiated planetary embryos. *Nat. Geosci.* 9, 781–785.
- Liles, D.C., de Villiers, J.P., 2012. Redetermination of the structure of 5C pyrrhotite at low temperature and at room temperature. *Am. Mineral.* 97 (2–3), 257–261. <http://dx.doi.org/10.2138/am.2012.3887>.
- Lorand, J.-P., Alard, O., 2010. Determination of selenium and tellurium concentrations in Pyrenean peridotites (Ariege, France): new insight into S/Se/Te systematics of the upper in mantle samples. *Chem. Geol.* 278 (1), 120–130.
- Lorand, J.-P., Luguët, A., Alard, O., 2013. Platinum-group element systematics and petrogenetic processing of the continental upper mantle: a review. *Lithos* 164, 2–21.
- Mahan, B., Siebert, J., Pringle, E.A., Moynier, F., 2017. Elemental partitioning and isotopic fractionation of Zn between metal and silicate and geochemical estimation of the S content of the Earth's core. *Geochim. Cosmochim. Acta* 196, 252–270. <http://dx.doi.org/10.1016/j.gca.2016.09.013>.
- Mann, U., Frost, D.J., Rubie, D.C., 2009. Evidence for high-pressure core-mantle differentiation from the metal-silicate partitioning of lithophile and weakly-siderophile elements. *Geochim. Cosmochim. Acta* 73 (24), 7360–7386. <http://dx.doi.org/10.1016/j.gca.2009.08.006>.
- Mao, H., Bell, P., Shaner, J.T., Steinberg, D., 1978. Specific volume measurements of Cu, Mo, Pd, and Ag and calibration of the ruby R1 fluorescence pressure gauge from 0.06 to 1 Mbar. *J. Appl. Phys.* 49 (6), 3276–3283.
- Mavrogenes, J.A., O'Neill, H.S., 1999. The relative effects of pressure, temperature and oxygen fugacity on the solubility of sulfide in mafic magmas. *Geochim. Cosmochim. Acta* 63 (7–8), 1173–1180. [http://dx.doi.org/10.1016/S0016-7037\(98\)00289-0](http://dx.doi.org/10.1016/S0016-7037(98)00289-0).
- McCoy, T.J., Dickinson, T.L., Lofgren, G.E., 1999. Partial melting of the indarch (EH4) meteorite: a textural, chemical, and phase relations view of melting and melt migration. *Meteorit. Planet. Sci.* 34 (5), 735–746.
- McDonough, W., Sun, S.-s., 1995. The composition of the Earth. *Chem. Geol.* 120 (3–4), 223–253. [http://dx.doi.org/10.1016/0009-2541\(94\)00140-4](http://dx.doi.org/10.1016/0009-2541(94)00140-4).
- McDonough, W.F., 2003. Compositional model for the Earth's core. In: *Treatise on Geochemistry*, vol. 2, p. 568.
- Morard, G., Andraut, D., Guignot, N., Siebert, J., Garbarino, G., Antonangeli, D., 2011. Melting of Fe–Ni–Si and Fe–Ni–S alloys at megabar pressures: implications for the core-mantle boundary temperature. *Phys. Chem. Miner.* 38 (10), 767–776. <http://dx.doi.org/10.1007/s00269-011-0449-9>.
- Morard, G., Katsura, T., 2010. Pressure-temperature cartography of Fe–S–Si immiscible system. *Geochim. Cosmochim. Acta* 74 (12), 3659–3667.
- Morard, G., Siebert, J., Andraut, D., Guignot, G., Garbarino, F., Guyot, F., Antonangeli, D., 2013. The Earth's core composition from high pressure density measurements of liquid iron alloys. *Earth Planet. Sci. Lett.* 373, 169–178. <http://dx.doi.org/10.1016/j.epsl.2013.04.040>.
- Morbidelli, A., Lunine, J., O'Brien, D., Raymond, S., Walsh, K., 2012. Building terrestrial planets. *Annu. Rev. Earth Planet. Sci.* 40 (1), 251–275.
- O'Neill, H., 1991. The origin of the Moon and the early history of the Earth a chemical model. Part 2: the Earth. *Geochim. Cosmochim. Acta* 55 (4), 1159–1172. [http://dx.doi.org/10.1016/0016-7037\(91\)90169-6](http://dx.doi.org/10.1016/0016-7037(91)90169-6).
- O'Neill, H.S., Eggins, S.M., 2002. The effect of melt composition on trace element partitioning: an experimental investigation of the activity coefficients of FeO, NiO, CoO, MoO₂ and MoO₃ in silicate melts. *Chem. Geol.* 186 (1–2), 151–181. [http://dx.doi.org/10.1016/S0009-2541\(01\)00414-4](http://dx.doi.org/10.1016/S0009-2541(01)00414-4).
- O'Brien, D.P., Walsh, K.J., Morbidelli, A., Raymond, S.N., Mandell, A.M., 2014. Water delivery and giant impacts in the grand tack scenario. *Icarus* 239, 74–84. <http://dx.doi.org/10.1016/j.icarus.2014.05.009>.
- Pradhan, G.K., Fiquet, G., Siebert, J., Auzende, A.-L., Morard, G., Antonangeli, D., Garbarino, G., 2015. Melting of MORB at core-mantle boundary. *Earth Planet. Sci. Lett.* 431, 247–255. <http://dx.doi.org/10.1016/j.epsl.2015.09.034>.
- Raymond, S.N., Quinn, T., Lunine, J.L., 2006. High-resolution simulations of the final assembly of Earth-like planets I: terrestrial accretion and dynamics. *Icarus* 183 (2), 265–282.
- Righter, K., Drake, M., Yaxley, G., 1997. Prediction of siderophile element metal-silicate partition coefficients to 20 GPa and 2800 °C: the effects of pressure, temperature, oxygen fugacity, and silicate and metallic melt compositions. *Phys. Earth Planet. Inter.* 100 (1–4), 115–134. [http://dx.doi.org/10.1016/S0031-9201\(96\)03235-9](http://dx.doi.org/10.1016/S0031-9201(96)03235-9).
- Rose-Weston, L., Brenan, J.M., Fei, Y., Secco, R.A., Frost, D.J., 2009. Effect of pressure, temperature, and oxygen fugacity on the metal-silicate partitioning of Te, Se, and S: implications for Earth differentiation. *Geochim. Cosmochim. Acta* 73 (15), 4598–4615. <http://dx.doi.org/10.1016/j.gca.2009.04.028>.
- Rubie, D., Melosh, H., Reid, J., Liebske, C., Righter, K., 2003. Mechanisms of metal-silicate equilibration in the terrestrial magma ocean. *Earth Planet. Sci. Lett.* 205 (3–4), 239–255. [http://dx.doi.org/10.1016/S0012-821X\(02\)01044-0](http://dx.doi.org/10.1016/S0012-821X(02)01044-0).
- Rubie, D.C., Laurenz, V., Jacobson, S.A., Morbidelli, A., Palme, H., Vogel, A.K., Frost, D.J., 2016. Highly siderophile elements were stripped from Earth's mantle by iron sulfide segregation. *Science* 353 (6304), 1141–1144. <http://dx.doi.org/10.1126/science.aaf6919>.
- Rubie, D.C., et al., 2011. Heterogeneous accretion, composition and core-mantle differentiation of the Earth. *Earth Planet. Sci. Lett.* 301 (1–2), 31–42. <http://dx.doi.org/10.1016/j.epsl.2010.11.030>.
- Rudge, J.F., Kleine, T., Bourdon, B., 2010. Broad bounds on Earth's accretion and core formation constrained by geochemical models. *Nat. Geosci.* 3 (6), 439–443.
- Savage, P.S., Moynier, F., Chen, H., Shofner, G., Siebert, J., Badro, J., Puchtel, I.S., 2015. Copper isotope evidence for large-scale sulphide fractionation during Earth's differentiation. *Geochim. Perspect. Lett.* 1, 53–64. <http://dx.doi.org/10.7185/geochemlet.1506>.

- Schönbächler, M., Carlson, R.W., Horan, M.F., Mock, T.D., Hauri, E.H., 2010. Heterogeneous accretion and the moderately volatile element budget of Earth. *Science* 328 (5980), 884–887.
- Seagle, C.T., Campbell, A.J., Heinz, D.L., Shen, G., Prakapenka, V.B., 2006. Thermal equation of state of Fe₃S and implications for sulfur in Earth's core. *J. Geophys. Res., Solid Earth* 111 (B6). <http://dx.doi.org/10.1029/2005JB004091>.
- Siebert, J., Badro, J., Antonangeli, D., Ryerson, F.J., 2012. Metal–silicate partitioning of Ni and Co in a deep magma ocean. *Earth Planet. Sci. Lett.* 321–322, 189–197. <http://dx.doi.org/10.1016/j.epsl.2012.01.013>.
- Siebert, J., Badro, J., Antonangeli, D., Ryerson, F.J., 2013. Terrestrial accretion under oxidizing conditions. *Science* 339 (6124), 1194–1197.
- Siebert, J., Malavergne, V., Guyot, F., Combes, R., Martinez, I., 2004. The behaviour of sulphur in metal–silicate core segregation experiments under reducing conditions. *Phys. Earth Planet. Inter.* 143, 433–443.
- Stevenson, D., 1990. Fluid dynamics of core formation. In: *Origin of the Earth*, vol. 1, pp. 231–249.
- Sylvester, P.J., Eggins, S.M., 1997. Analysis of Re, Au, Pd, Pt and Rh in NIST glass certified reference materials and natural basalt glasses by laser ablation ICP-MS. *Geostand. Newsl.* 21 (2), 215–229. <http://dx.doi.org/10.1111/j.1751-908X.1997.tb00672.x>.
- Thomen, A., Robert, F., Remusat, L., 2014. Determination of the nitrogen abundance in organic materials by NanoSIMS quantitative imaging. *J. Anal. At. Spectrom.* 29 (3), 512–519. <http://dx.doi.org/10.1039/C3JA50313E>.
- Wade, J., Wood, B., 2005. Core formation and the oxidation state of the Earth. *Earth Planet. Sci. Lett.* 236 (1–2), 78–95. <http://dx.doi.org/10.1016/j.epsl.2005.05.017>.
- Wade, J., Wood, B.J., Tuff, J., 2012. Metal–silicate partitioning of Mo and W at high pressures and temperatures: evidence for late accretion of sulphur to the Earth. *Geochim. Cosmochim. Acta* 85, 58–74. <http://dx.doi.org/10.1016/j.gca.2012.01.010>.
- Walker, R.J., 2009. Highly siderophile elements in the Earth, Moon and Mars: update and implications for planetary accretion and differentiation. *Chem. Erde-Geochem.* 69 (2), 101–125.
- Wang, Z., Becker, H., 2013. Ratios of S, Se and Te in the silicate Earth require a volatile-rich late veneer. *Nature* 499 (7458), 328–331.
- Wang, Z., Laurenz, V., Petitgirard, S., Becker, H., 2016. Earth's moderately volatile element composition may not be chondritic: Evidence from In, Cd and Zn. *Earth Planet. Sci. Lett.* 435, 136–146. <http://dx.doi.org/10.1016/j.epsl.2015.12.012>.
- Watson, E.B., 1994. Diffusion in volatile-bearing magmas. *Rev. Mineral. Geochem.* 30 (1), 371–411.
- Wohlert, A., Wood, B.J., 2015. A Mercury-like component of early Earth yields uranium in the core and high mantle ¹⁴²Nd. *Nature* 520 (7547), 337–340.
- Wood, B.J., 2008. Accretion and core formation: constraints from metal–silicate partitioning. *Philos. Trans. R. Soc. Lond. A, Math. Phys. Eng. Sci.* 366 (1883), 4339–4355. <http://dx.doi.org/10.1098/rsta.2008.0115>.
- Wood, B.J., Halliday, A.N., 2005. Cooling of the Earth and core formation after the giant impact. *Nature* 437 (7063), 1345–1348.